

Magneto-electronic properties of Gd-implanted tetrahedral amorphous carbon

Li Zeng(曾立)*

NSF NSEC Center, 3112 Etcheverry Hall, University of California–Berkeley, Berkeley, California 94720, USA

H. Zutz

II. Institute of Physics, University of Göttingen, Friedrich-Hund-Platz 1, 37077 Göttingen, Germany

F. Hellman

Department of Physics, University of California–Berkeley, Berkeley, California 94720, USA

E. Helgren

Department of Physics, California State University–East Bay, Hayward, California 94542, USA

J. W. Ager III

Lawrence Berkeley National Laboratory, Berkeley, California 94720, USA

C. Ronning

Institute for Solid State Physics, University of Jena, Max-Wien-Platz 1, 07743 Jena, Germany

(Received 31 January 2011; revised manuscript received 16 August 2011; published 14 October 2011)

The structural, electronic, magnetic, and magneto-electronic properties of tetrahedral amorphous carbon (*ta*-C) thin films doped with gadolinium via ion implantation ($ta\text{-C}_{1-x}:\text{Gd}_x$, $x = 0.02 \sim 0.20$) have been studied, both as prepared and after annealing, with Xe-implanted samples as control samples. Gd implantation causes significant increases in electrical conductivity, showing that Gd adds carriers as in other rare earth–semiconductor systems. Gd also provides a large local moment from its half-filled *f* shell. Carrier-mediated Gd-Gd interactions are strong but very frustrated, causing a spin-glass state < 10 K for higher x . An enormous negative magnetoresistance (about -10^3 at 3 K in a 70-kOe field for $x = 0.088$) is observed at low T (< 30 K), an indication of carrier–moment interactions that cause magnetic disorder–induced localization and consequent magnetic field–induced delocalization as Gd moments align with the magnetic field. Gd implantation causes substantial changes in Raman intensity, associated with conversion of C-C bonds into Raman inactive bonds, which induce further graphitization after annealing. The changing nature of the C-C bonding with increasing x or with annealing causes the electrical transport properties to depend on Gd concentration x with a nonmonotonic dependence. Systematic but nonmonotonic trends are seen on comparing the magnetic and magnetotransport properties of Gd-doped *a*-C, *a*-Si, and *a*-Ge matrices, suggesting that electron concentration and band gap play separate important roles.

DOI: [10.1103/PhysRevB.84.134419](https://doi.org/10.1103/PhysRevB.84.134419)

PACS number(s): 61.72.U–

I. INTRODUCTION

Carbon exists in many structures, and C-based materials possess many remarkable properties. For amorphous carbon (*a*-C), its properties vary between graphitic and diamondlike depending on the fraction of sp^2 - and sp^3 -bonded carbon atoms. Systems with a large fraction of sp^3 bonds are known as tetrahedral amorphous carbon (*ta*-C) and have many properties similar to those of the diamond. The growth of *ta*-C was explored in the late 1990s, and the nucleation and growth mechanisms are mostly understood.¹ The most recent *ta*-C research is aimed at preserving diamondlike properties while incorporating suitable impurities for novel optical, electrical, or magnetic properties for potential applications. *ta*-C can be doped with low concentrations of rare earth elements (between 10^{17} and 10^{19} cm^{-3}),² yielding a material that shows sharp luminescence lines over the whole UV–visible–infrared range due to the intra- $4f$ luminescence of the lanthanides. This feature, together with high hardness, makes the material appealing for optoelectronic devices. Rare earth elements also possess magnetic properties that, if incorporated at high

concentrations into suitable semiconducting carbon matrices, offer a potential high-hardness, magnetic semiconductor, with a high intrinsic band gap, like Gd-doped GaN.³

This study focuses on the magnetic and magneto-electronic properties of *ta*-C doped with Gd via ion implantation. Gd is nearly always a trivalent ion, with a half-filled *f* electron shell, thus providing three electron carriers and a large local moment ($J = S = 7/2$). The previously studied amorphous magnetic semiconductor systems' *a*-Gd_{*x*}Si_{1–*x*}, *a*-Gd_{*x*}Ge_{1–*x*} and *a*-Gd_{*x*}Y_{*y*}Si_{1–*x*–*y*} films have shown a remarkable set of magneto-electronic properties, including enormous negative magnetoresistance (MR, e.g., 10^5 at 1 K and 1% at 90 K in a 60-kOe field).^{4,5} In those materials, significant carrier–moment interactions lead to carrier-mediated Gd-Gd interactions, producing a spin-glass (SG) ground state, unsaturated magnetization at high field, and negative MR. MR and all carrier–moment effects decrease with increasing x , are smaller in *a*-Gd_{*x*}Ge_{1–*x*} compared to *a*-Gd_{*x*}Si_{1–*x*}, and are reduced with increasing nonmagnetic Y at constant Gd x , all effects attributed to electrical screening (associated with increased

electron concentration due to either increasing x or y (at fixed Gd moment concentration x) or the smaller band gap of Ge compared to Si (at a given x).⁶

Based on those studies, we suggest that the magnitude and temperature range of the negative MR increase with an increasing band gap, suggesting the desirability of a higher band gap matrix such as carbon, the first element in group IV. The uniqueness of carbon among other group-IV semiconductors is its stable sp^2 configuration vs metastable sp^3 configuration, therefore offering a (desirable) tunability of band gap via tuning the sp^3/sp^2 ratio but also the potential complexity of different local electron wave functions. Previous studies have shown that Gd-doped a -C, prepared via cosputtering, is mostly sp^2 bonded and thus exhibits only a small band gap; still, a large negative MR was found at low temperature, comparable to that of a -Gd $_x$ Si $_{1-x}$, but vanishes by ~ 30 K, significantly lower than in a -Gd $_x$ Si $_{1-x}$, which is consistent with the preceding expectation regarding the effect of reduced band gap.⁷ By contrast, the ta -C band gap can be as high as 2.5 eV with high sp^3/sp^2 ratio,⁸ thus providing a new starting matrix to study the moment and carrier interactions induced by Gd. After Gd incorporation, the physical properties (electrical, magnetic, and magnetotransport properties) of the resulting ta -C:Gd system are shown to depend strongly on the interactions between the magnetic dopant and the electrons in the carbon matrix; this matrix, however, we found has been affected by the Gd incorporation (significantly different from that for the control implantation of Xe) such that for moderate x , it is no longer ta -C.

II. EXPERIMENTAL METHODS

Thin ta -C films with high sp^3 fraction ($\sim 80\%$) have been prepared by mass-selected ion beam deposition.⁹ Briefly, carbon ions are accelerated to 30 keV, mass separated, and finally decelerated down to 100 eV prior to deposition onto amorphous SiN $_x$ -coated Si substrates held at room temperature (RT). The thicknesses of the ta -C films were between 40 and 60 nm. Such films exhibit diamondlike properties, including high hardness, high resistivity, and a band gap of ~ 2.5 eV.¹

The ta -C samples were implanted at RT with ^{155}Gd ions using ion energy of 50 keV and varying ion fluence to give different Gd-doping concentrations x . Double-energy (30 and 50 keV) implantations were also carried out to achieve a more uniform Gd-doping depth profile. Details of the parameters and samples are listed in Table I. The ion range and resulting film compositions were calculated using the program package Transport of Ions in Matter (TRIM),¹⁰ and verified by Rutherford backscattering (RBS) measurements analyzed by the Rutherford Universal Manipulation Program (RUMP) analysis package.¹¹ For all films in this work, either singly or doubly implanted, the Gd concentration is approximated as a single layer with concentration x and thickness t based on RBS-RUMP analysis, with t either 8 or 20 nm (depending on implantation energy used in single vs double implant) and x between 0.022 and 0.20 (depending on Gd ion fluence). An example of this analysis is shown and discussed later.

Annealing studies were performed ≤ 550 °C in a rapid thermal annealer (RTA) with forming gas (5% H $_2$ /95% N $_2$) to avoid oxidation. The temperature profile for annealing

TABLE I. ta -C $_{1-x}$:Gd $_x$ sample information. Single-energy implantation is above the line; double-energy implantation is below the line.

x^a	ta -C thickness (nm)	^{155}Gd fluence (10^{15} ion/cm 2)	Gd energy (keV)	p_{eff}^b (μ_B)	θ^b (K)	σ_{RT}^c [$(\Omega\text{-cm})^{-1}$]
0.040	42	5.0	50	8.54	0.6	249.3
0.070	42	9.5	50	9.35	-0.7	527.9
0.200	42	40	50	8.80	5.66	312.2
0.022	43	2.5 + 3.25	30 + 50	9.02	-0.4	39.7
0.088	61	10 + 13	30 + 50	8.88	-1.6	253.6
0.176	43	20 + 26	30 + 50	8.12	2.56	161.0

^aObtained from RUMP (Ref. 11) simulation of RBS data, assuming a simple trilayer model as described in the text.

^b p_{eff} per Gd obtained from measured magnetic susceptibility $\chi(T)$ fit to $A/(T - \theta)$, where θ is the CW temperature and the CW constant $A = n_{\text{Gd}}(p_{\text{eff}}\mu_B)^2/(3k_B)$.

^c σ_{RT} , room temperature conductivity.

consisted of three stages: a 2-min. temperature rise, a 1-min. temperature soak, and an exponential temperature decay back to RT. Carbon bonding information was determined by Raman spectra using a 488-nm laser and a SPEX 1877 0.6-m triple spectrometer. Direct current (DC) electrical transport was measured using a standard four-point-probe method with conducting silver paint strips as electrical contacts. Sample magnetization M as a function of both temperature T and field H and magnetoelectronic properties were measured in a Quantum Design magnetometer (with a resistivity probe for the transport and magnetotransport data). Representative samples (as deposited and after annealing) were prepared for cross-section transmission electron microscopy (TEM) using a focused ion beam (FIB) setup (Nova Nanolab 600, FEI) and analyzed using a Philips CM200-FEG-UT TEM.

A set of Xe-implanted ta -C films (ta -C $_{1-x}$:Xe $_x$) were prepared under identical implantation and annealing conditions to be used as control samples to monitor the effects of implantation damage. Xe and Gd ions have almost identical radii and similar masses; therefore, the implantation damage created in the ta -C matrix is similar for both sets of samples. Xe has a closed-shell electron structure and thus is chemically, magnetically, and electrically inert. Therefore, observed electrical or magnetic differences between ta -C $_{1-x}$:Gd $_x$ and ta -C $_{1-x}$:Xe $_x$ are due to Gd incorporation. We measured Xe-implanted control samples to eliminate contributions from radiation damage to the transport, magnetization, and magnetotransport properties. More sample information is displayed in Table I, and more experimental details are available in Ref. 7.

III. EXPERIMENTAL RESULTS

A. Structural characterization

Figure 1(a) shows a TRIM simulation of a typical double-energy implantation of Gd ions into ta -C. The final ion distribution is the superposition of two Gaussian distributions from two consecutive single-energy implantations with

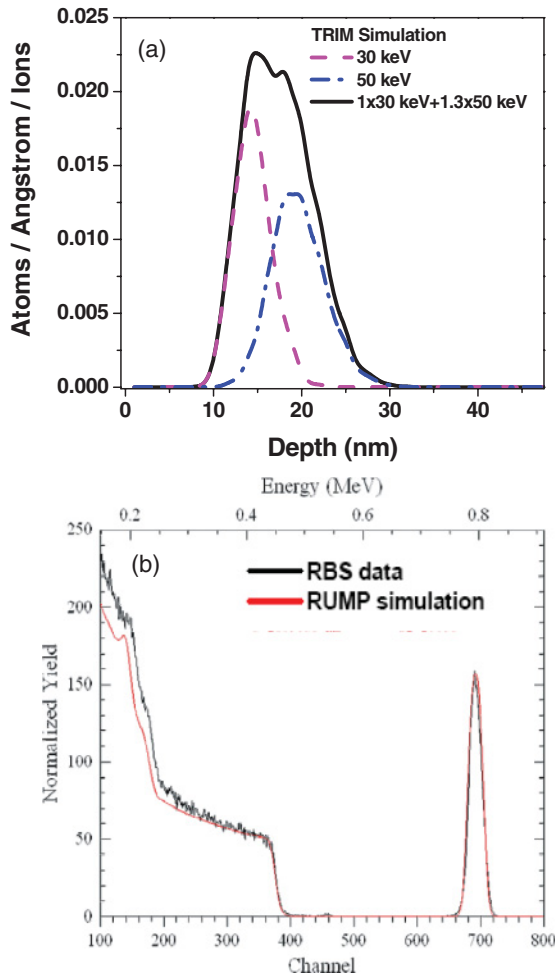


FIG. 1. (Color online) (a) TRIM simulation of double-energy (30 + 50 keV) implantation of *ta*-C with a density of 3 g/cm³, revealing a more uniform depth profile from the overlapping of two Gaussian-type single-energy implantation profiles. (b) RBS data and RUMP simulation for a double-energy implanted sample with two ion fluences of 1×10^{16} ion/cm² (30 keV) and 1.3×10^{16} ion/cm² (50 keV). The best fit was obtained using a simple layered structure: undoped *ta*-C(5 nm)/*ta*-C_{0.912}Gd_{0.088}(20 nm)/*ta*-C(36 nm).

different ion energies, giving a more uniform doping depth profile than a single implantation. Figure 1(b) shows a representative RBS spectrum for a double-implanted sample (*ta*-C_{0.912}Gd_{0.088}), corresponding to the TRIM-simulated distribution in Fig. 1(a). The total ion fluence for this sample was high (2.3×10^{16} ion/cm²); thus, sputtering of the surface is significant and results in a reduction of the undoped surface layer to ~ 5 nm compared to ~ 10 nm for low ion fluence implantations. The analysis of the RBS spectrum by RUMP uses a simple trilayer model, including a surface C layer, a doped *ta*-C_{1-x}Gd_x layer, and a deeper undoped C layer. This analysis confirmed the TRIM simulations, both in depth and in doping profile, including the thickness of the undoped surface layer for all samples. For analysis of both single- and double-energy implanted samples, we refer to the RUMP simulation results of the RBS data for Gd concentration *x*, as well as film thickness *t*, which is ~ 8 and ~ 20 nm for the single- and double-energy implanted samples, respectively.

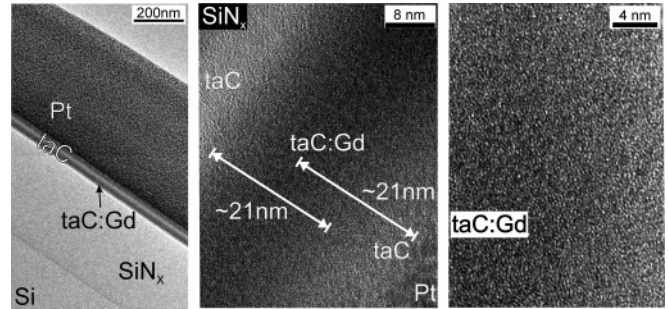


FIG. 2. Three representative cross-section TEM images for Gd-implanted *ta*-C, implanted with the highest total ion fluence. The left picture shows an overview of the whole film. The Pt top layer originates from the FIB preparation process. The middle micrograph shows a magnification of the implanted film. The SiN_x substrate is in the left upper part and the surface of the *ta*-C film is in the right bottom part of the micrograph. The Gd-containing layer is clearly visible by the strong contrast change induced by the high Z of Gd. The right picture is an HR-TEM zoom-out image of the center Gd layer: No crystalline clusters or precursor lattice fringes are visible.

This trilayer analysis affects the absolute value of conductivity but not MR (which is normalized to zero-field conductivity) or magnetization (which depends only on the total number of Gd atoms, a known value based on either implantation fluence or RBS integration, which agree with each other).

High-resolution-transmission electron microscopy (HR-TEM) was performed on representative samples to determine whether Gd-C clusters or crystallites are formed by the implantation process and whether the *ta*-C:Gd structure remains amorphous. The left overview picture in Fig. 2 confirms the trilayer TRIM simulation, including the presence of the undoped surface layer. The middle picture in Fig. 2 shows the cross section of the sample with the highest Gd concentration (*ta*-C_{0.80}Gd_{0.20}). The right picture in Fig. 2 is a high-resolution micrograph of the center region of this high doping sample. No crystallites, clusters, or precrystallite lattice fringes are observed in any HR-TEM image. We concluded that the samples remain amorphous within the resolution of the HR-TEM, and if clusters are present, they are well < 2 nm in size. Several samples were annealed ≤ 550 °C; HR-TEM on these samples showed only an amorphous structure with no signs of cluster formation or Gd, Gd-C, or C-C crystallites.

Raman spectroscopy was used to obtain information on the carbon bonding before and after Gd/Xe implantation, as well as after annealing. Two major Raman active modes correspond to the breathing mode of disordered graphitic six-member rings (the *D* peak, ~ 1350 cm⁻¹) and the stretching mode of C-C pairs (the *G* peak, ~ 1580 cm⁻¹). Using the integrated peak intensity ratio I_D/I_G (both peaks fit with Gaussian functions) and the three-stage model for *a*-C Raman spectroscopy,¹² we estimated the sp^2/sp^3 ratio for these films.

The Raman spectra of undoped, as-grown *ta*-C films with a high sp^3 fraction show a dominant *G* peak due to the lack of graphitic ring sites; thus, a very small I_D/I_G ratio (< 1). Annealing ≤ 550 °C in an inert environment has little influence on the Raman spectra, consistent with Refs. 1 and 13. The strong sp^3 covalent bonds, once formed, are very stable under thermal treatments, since the energy barrier for converting sp^3

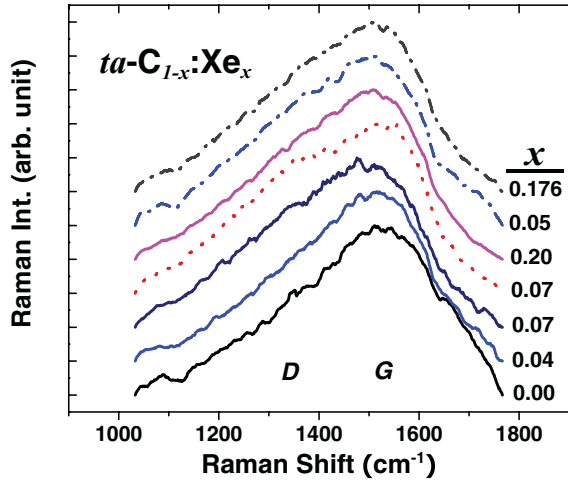


FIG. 3. (Color online) Raman spectra of pure *ta-C* and *ta-C*_{1-*x*}:*Xe*_{*x*} thin films. Solid lines represent spectra of single-energy implanted samples; dash dotted lines are spectra of double-energy implanted samples. The dotted line shows for comparison a Raman spectrum of an annealed sample with *x* = 0.07. Data are normalized to peak intensity and offset from one another for clarity.

to *sp*² is large (oxygen can act as a catalyst to lower this barrier; thus, annealing in vacuum or an inert gas is essential). Diamond can be annealed in vacuum at a temperature as high as 1800 K without graphitization (see Sec. 13.3 of Ref. 14). There is, however, a small increase of the *I*_D/*I*_G ratio for these annealed *ta-C* films, presumably due to the graphitization of the <20% *sp*²-bonded carbon chains in as-grown *ta-C* films.

Figure 3 shows the normalized Raman spectra of all *ta-C*_{1-*x*}:*Xe*_{*x*} thin films with increasing implantation fluence. The change in the spectral shape is small. The *I*_D/*I*_G ratio increases slightly, ≤2.3, and is almost independent of *Xe* fluence. Therefore, we concluded that the change of the matrix caused by the energetic *Xe* implantation process is small for these as-implanted control samples: a small fraction of *sp*³ bonds have been converted to *sp*² bonds. These results are in agreement with a study on radiation-induced transformation of diamond.¹⁵

Figure 4 shows the Raman spectra of all *ta-C*_{1-*x*}:*Gd*_{*x*} thin films, where the peak height was normalized to emphasize the change in line shape. In contrast to the *ta-C*_{1-*x*}:*Xe*_{*x*} samples, there is a noticeable shift of spectral weight to lower wavenumbers (toward the *D* position) and a pronounced change in line shape for the highest *Gd* concentrations. For *x* = 0.20 (single-energy implanted) and *x* = 0.176 (double-energy implanted), a broad peak with very low Raman intensity is observed, and the peak maximum is shifted to a much lower wavenumber. Fitting to two peak profiles to simulate the *D* and *G* modes is impossible for these samples.

Figure 5 shows the unnormalized Raman spectra of the single-energy implanted *ta-C*_{1-*x*}:*Gd*_{*x*} films. The inset shows the total Raman intensities (*I*_D + *I*_G) of both the *Gd*- and the *Xe*-implanted samples. For the *ta-C*_{1-*x*}:*Xe*_{*x*} films, the total Raman intensity is only slightly lower than for the pure *ta-C* and almost independent of *Xe* fluence, similar to the *x* dependence of its *I*_D/*I*_G ratio. However, the Raman intensity of the *ta-C*_{1-*x*}:*Gd*_{*x*} films decreases monotonically

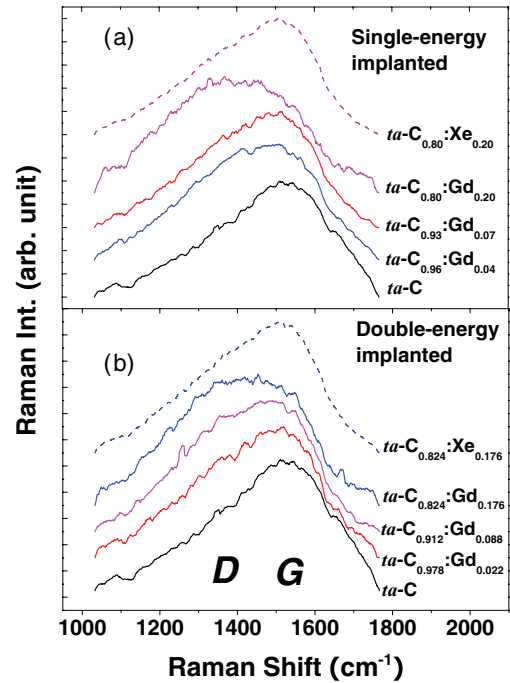


FIG. 4. (Color online) Raman spectra of *ta-C*_{1-*x*}:*Gd*_{*x*} thin films, which were prepared by (a) single-energy implantation or (b) double-energy implantation. The two dashed lines are control spectra of samples implanted with high fluences of *Xe*. Note the apparent difference between the *ta-C*_{1-*x*}:*Gd*_{*x*} and the *ta-C*_{1-*x*}:*Xe*_{*x*} Raman spectra.

and dramatically with increasing *x*. This suggests that the incorporated *Gd* atoms convert local bonds into Raman inactive bonds in this energy range. This low Raman intensity supports the HR-TEM results that show carbon atoms are not clustering; otherwise, a more Raman-active carbon matrix would be seen.

After rapid thermal annealing to 550 °C, the *D* and *G* peaks in *Gd*-implanted films become more pronounced and the

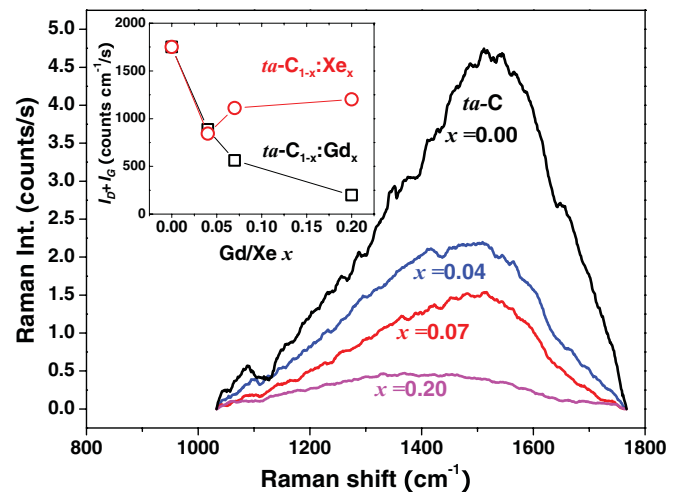


FIG. 5. (Color online) Unnormalized Raman spectra of single-energy *Gd*-implanted *ta-C* thin films with increasing concentration. The inset shows the observed peak intensity (*I*_D + *I*_G) vs *x* for both *ta-C*_{1-*x*}:*Xe*_{*x*} and *ta-C*_{1-*x*}:*Gd*_{*x*} samples.

I_D/I_G ratio of the implanted samples increases ≤ 8 for both the Xe- and the Gd-implanted films (see, e.g., Fig. 3, dotted line), which was not the case for the unimplanted *ta*-C films. This can be understood by graphitization of the implantation-induced damage centers, which include vacancies, interstitials, dangling bonds, and defect clusters. Although there is some initial graphitization upon RT implantation, most damage centers are “frozen” and bond rearrangement is unlikely at this low temperature. However, during annealing at sufficiently high temperatures, vacancies and interstitials become mobile, and local bond rearrangement is possible. This results in the formation of more stable sp^2 -bonded graphitic sites, which gives rise to a more intense Raman *D* line and thus, as observed, a much larger I_D/I_G ratio after annealing.

B. Magnetization

The Xe-implanted *ta*-C samples show no magnetic signal above the superconducting quantum interference device detection limit (10^{-7} emu) at any temperature; thus, all observed magnetization in *ta*-C $_{1-x}$:Gd $_x$ films is due to Gd incorporation. For Gd-implanted *ta*-C with $x \leq 0.07$, $M(H,T)$ follows the pure paramagnetic $J = 7/2$ Brillouin function. The low-field (100 Oe) magnetic susceptibility $\chi(T)$ fits a Curie-Weiss (CW) law down to 2 K (the lowest measured temperature) with very small CW temperature $|\theta| < 1$ K. At higher $x > 0.088$, $\chi(T)$ shows increasing θ (≤ 5 K) and by $x = 0.176$, $\chi(T)$ shows clear SG freezing, as indicated by a split between zero-field-cooled (ZFC) and field-cooled (FC) $\chi(T)$. Figure 6 shows $\chi(T)$ for the double-energy implanted *ta*-C $_{0.824}$ Gd $_{0.176}$ sample. The SG freezing temperature T_f estimated from the splitting between the ZFC and the FC data is 5 K (alternating current susceptibility measurements were not made for these samples, but extensive previous work on the related system *a*-Gd $_x$ Si $_{1-x}$ shows classic SG behavior in $\chi(T)$, see Refs. 16 and 17). For all *ta*-C $_{1-x}$:Gd $_x$ samples, the CW fits of the paramagnetic state $\chi(T)$ (for high x , at $T > T_f$) reveal effective moments p_{eff} between 8.1 and 9.4 μ_B per Gd atom (as shown in

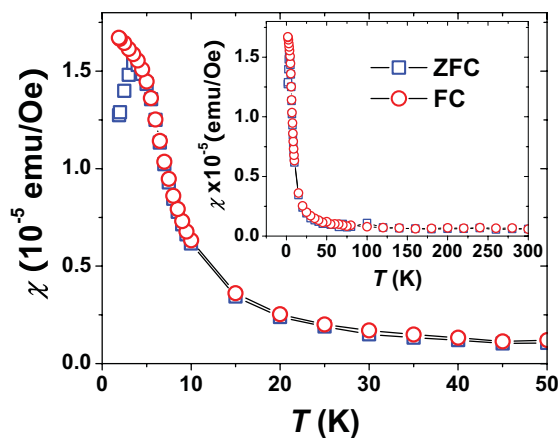


FIG. 6. (Color online) ZFC and FC DC susceptibility χ vs T for the double-energy implanted *ta*-C $_{0.824}$ Gd $_{0.176}$ sample showing SG freezing (measured at the DC applied magnetic field of ~ 100 Oe). The inset shows expanded the temperature range of $\chi(T)$, which follows the CW law with small (2.5 K) θ and p_{eff} of 8.12, determined from $\chi(T) > T_f$.

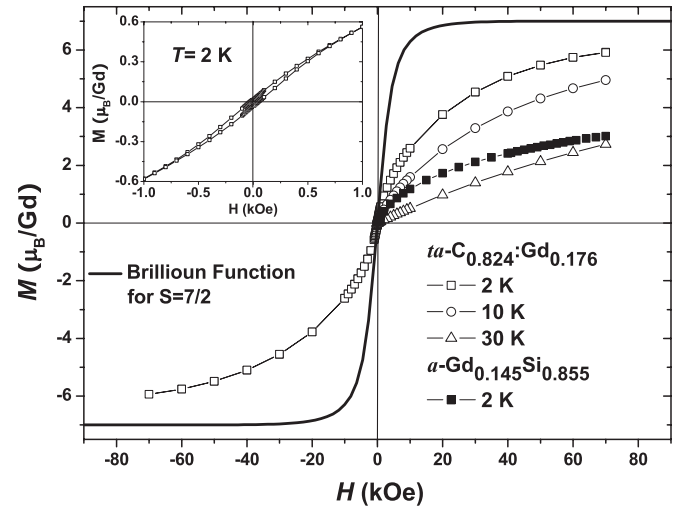


FIG. 7. M vs H data for the double-energy implanted *ta*-C $_{0.824}$ Gd $_{0.176}$ sample at various T . The inset shows a hysteresis loop at 2 K ($< T_f$). $M(H)$ at $T = 2$ K for a cosputtered *a*-Gd $_{0.13}$ Si $_{0.87}$ film is also plotted for comparison. The Brillouin function for $J = 7/2$ at 2 K is shown as a solid line. For these data, the total implant dose was used to give the number of Gd atoms needed for converting measured total m to the intrinsic M , requiring no assumption about film thickness or density.

Table I) and low θ values. For a free Gd $^{3+}$ ion, $p_{\text{eff}} = 7.9 \mu_B$ and typical Gd-based amorphous materials have $p_{\text{eff}} \sim 8.5 \mu_B$ and $\theta > T_f$. The enhanced p_{eff} often found in Gd-based materials is attributed to polarization of *s* electrons by the *s*-*f* exchange interaction, which is also responsible for the carrier-mediated Ruderman-Kittel-Kasuya-Yosida (RKKY) interactions seen for Gd metal and alloys, which leads to SG freezing and large θ for moderate x .^{6,16}

Figure 7 shows the magnetic field dependence $M(H)$ of the same double-energy implanted *ta*-C $_{0.824}$ Gd $_{0.176}$ sample at various T . $M(H)$ is suppressed well below the Brillouin function for free $J = S = 7/2$ ions, consistent with the observed SG freezing and again indicative of the presence of strong magnetic interactions. The *f* shell of Gd is sufficiently well shielded, and the distance between Gd ions (even in pure Gd) is sufficiently large so that only a conduction electron-mediated interaction (which we call RKKY-like, for lack of a better term, in this amorphous structure) is a viable candidate to produce the strong Gd-Gd interactions we observed (e.g., lack of saturation of $M(H)$ even at low T and high field). The data show a small hysteresis loop at 2 K (vanishes at $H > 1000$ Oe or $T > T_f$), also consistent with the SG freezing behavior seen in the $\chi(T)$ data in Fig. 6. Based on the magnitude of suppression of $M(H,T)$ below the Brillouin function, the strength of the frustrated antiferromagnetic interactions in *ta*-C $_{1-x}$:Gd $_x$ are comparable to those in cosputtered *a*-Gd $_x$ C $_{1-x}$ ⁷ and in *a*-Gd $_x$ Ge $_{1-x}$ ⁶ but weaker than those in cosputtered *a*-Gd $_x$ Si $_{1-x}$,¹⁸ for which a representative data set (solid squares, for *a*-Gd $_{0.145}$ Si $_{0.855}$) at 2 K is included in Fig. 7 for a direct comparison.

C. Electrical transport and magnetotransport

Figure 8 shows temperature dependence of DC conductivity $\sigma(T)$ for all as-implanted *ta*-C $_{1-x}$:Gd $_x$ films. As discussed

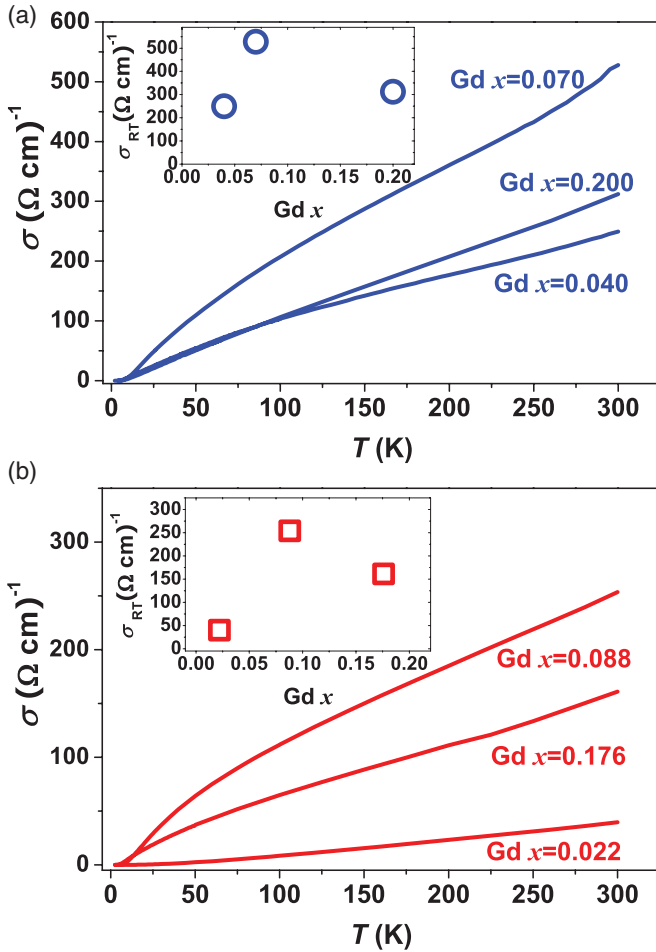


FIG. 8. (Color online) Conductivity $\sigma(T)$ for (a) single-energy implanted and (b) double-energy implanted samples. Insets show σ_{RT} as a function of x . σ_{RT} for undoped $ta-C$ is $10^{-9}(\Omega\text{-cm})^{-1}$.

earlier, we approximate the profile as a homogeneous buried doped layer with Gd concentrations and thicknesses from RUMP analysis of RBS data. Using this method, the RT conductivity (σ_{RT}) of $ta-C_{1-x}:Gd_x$ samples falls in the same range as fully homogeneous, codeposited amorphous metal semiconductor alloys, e.g., $a-Gd_xC_{1-x}$,⁷ $a-Gd_xSi_{1-x}$,^{4,5} and $a-Gd_xGe_{1-x}$.⁶ σ_{RT} is extremely low before implantation [$\sigma(295\text{ K}) \approx 10^{-9}(\Omega\text{-cm})^{-1}$ for virgin $ta-C$ films] and is increased orders of magnitude after Gd implantation [$\sim 10^2(\Omega\text{-cm})^{-1}$]. Xe-implanted $ta-C_{1-x}:Xe_x$ control samples were also prepared and measured; implanting Xe also increases σ_{RT} , but it does so two orders of magnitude *less* at RT than for the same dose of Gd (the difference in σ is much greater at low T). This difference is true even for implantation fluence exceeding the critical dose ($D_c \approx 3 \times 10^{14}$ atoms/cm³) to form a percolation path between the damage centers in $ta-C_{1-x}:Xe_x$, consistent with the known low radiation-induced density of states at the Fermi level in diamond [$N(E_F) \approx 10^{19}$ states/eV·cm³].¹⁵ Therefore, the dominant contribution to σ for $ta-C_{1-x}:Gd_x$ is from Gd doping ($\sim 3e^-$ per Gd^{3+} ion), i.e., the formation of a dopant band, and implantation-induced conducting centers of the $ta-C$ matrix contribute only secondary effects. The large σ_{RT} indicates a large number of carriers near the Fermi surface, subject to strong localization effects due to disorder.

A concentration-driven metal-to-insulator ($M-I$) transition is commonly observed in both amorphous metal semiconductor alloys and crystalline doped semiconductors. The term *metal-to-insulator* refers to the $T = 0$ K conductivity, which is finite for metals and zero for insulators. Figure 8 shows that as T is decreased, all $ta-C_{1-x}:Gd_x$ samples are on the insulating side of the $M-I$ transition, since $\sigma(T \rightarrow 0\text{ K}) \rightarrow 0$ even for $x = 0.20$, much higher than the critical concentration $x_C \approx 0.14$ found in other Gd-doped amorphous semiconductors. The insets in Fig. 8 show that σ_{RT} increases with x for $x \leq 0.088$ but then *decreases* for $x > 0.088$ for both the single and the double-energy implanted samples. This nonmonotonic concentration dependence of σ is different from what was seen in $a-Gd_xSi_{1-x}$ and $a-Gd_xGe_{1-x}$, where a monotonic increase in σ_{RT} was found, passing smoothly through the insulator to metal transition, for $x \leq 0.25$ (above which TEM showed signs of Gd clustering). However, it is similar to what was observed in sputtered $a-Gd_xC_{1-x}$ films, where the nonmonotonic dependence was attributed to a competition between increasing dopant concentration and increasing modifications to the C-matrix.⁷ Still, unlike sputtered $a-Gd_xC_{1-x}$ films, no correlation between the I_D/I_G ratio and σ_{RT} as a function of x is found. This nonmonotonic conductivity dependence on x is discussed later.

For three-dimensional (3D) insulating materials, $\sigma(T)$ is expected to be exponentially dependent on T , with exponent $\alpha = 1/4$, $1/2$, or 1 , corresponding to different transport mechanisms: 3D Mott-type variable range hopping (VRH), Efros-Shklovskii (ES)-type VRH, or single-activation energy hopping, respectively. The best fit for these data is found for $\alpha = 1/2$ consistent with ES-type VRH (a model that incorporates strong electron-electron interactions, as well as the effects of disorder in the transport process), as for other Gd-doped amorphous semiconductors. Figure 9 shows $\sigma(T)$ plotted on a logarithmic scale vs $T^{-\alpha}$ with $\alpha = 1/2$. On annealing, the matrix itself becomes significantly conducting and actually metallic (nonthermally activated) at low T but with low and complicated $\sigma(T)$.

Figure 9 also shows $\sigma(T)$ in 70-kOe field applied parallel to the plane of the film and the current direction (previous work on $a-Gd-Si$ alloys investigated the effect of different field directions and has shown it to be insignificant, not surprisingly for Gd-based 3D materials, which have little magnetic anisotropy). This sample, and all other $ta-C_{1-x}:Gd_x$ samples, shows an enormous increase in conductivity with applied field, i.e., a very large negative MR (e.g., -10^3 at 3 K in a 70-kOe field for $x = 0.088$), where MR is defined as usual as $\Delta p/p(H)$, and $MR = -MG$ (magnetoconductance) = $\Delta\sigma/\sigma(H = 0)$, where $\Delta\sigma = \sigma(H) - \sigma(H = 0)$. This conductivity increase can be understood in a modification of an Anderson localization model in which the applied magnetic field increases the localization length of the electrons by aligning Gd moments, therefore reducing one type of disorder seen by the electron carriers (magnetic disorder due to $s-f$ exchange coupling between the electron carriers and the randomly oriented local f states of Gd ions). The zero-field and high-field data in Fig. 9 converge at a temperature we call T' ; this temperature is taken as the temperature below which the effect of the Gd magnetic moments becomes important to the conductivity. No significant signature in any magnetic

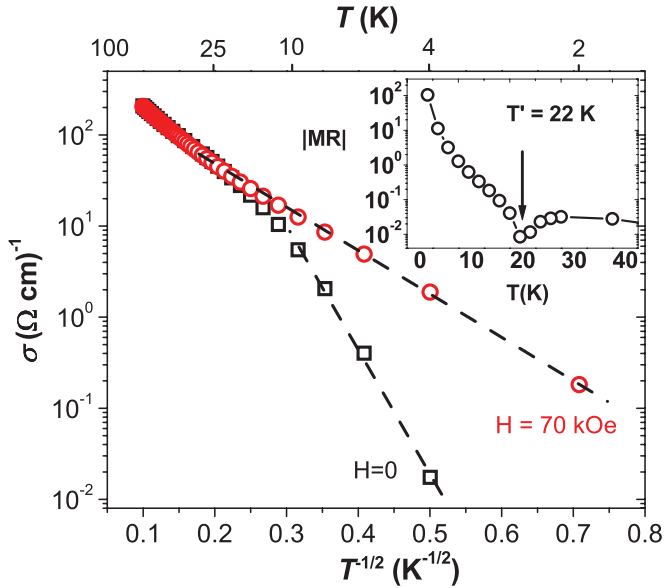


FIG. 9. (Color online) Conductivity $\sigma(T)$ as a function of $T^{-1/2}$ for the single-energy implanted $x = 0.07$ sample at 0 and 7 T. The two data sets converge at approximately 22 K, which is taken as the onset of the effect of the Gd moments on conductivity. The inset shows T dependence of absolute values of MR [$\text{MR} = \Delta\rho/\rho(H) = -MG = \Delta\sigma/\sigma(H = 0)$, where $\Delta\sigma = \sigma(H) - \sigma(H = 0)$ and $\Delta\rho = \rho(H) - \rho(H = 0)$] to show both negative MR and positive MR and the temperature T' defined as the temperature where MR crosses through 0.

property has yet been found at this temperature (for any of the many Gd-based amorphous semiconductor systems yet studied), which is therefore taken to represent a crossover below which moment-carrier interactions become a dominant effect in transport. T' is discussed further and more carefully defined later.

IV. DISCUSSION

Raman line shapes and the I_D/I_G ratios indicate that after implantation, the matrix of the $ta\text{-C}_{1-x}\text{:Gd}_x$ films has lost some of its sp^3 -bonded character but is still much less graphitic than cosputtered $a\text{-Gd}_x\text{C}_{1-x}$ films. For cosputtered $a\text{-Gd}_x\text{C}_{1-x}$ thin films, Raman spectra show a distinct D peak corresponding to the disordered sp^2 -bonded graphitic rings and the I_D/I_G ratio can be as high as 12 (for $x = 0.11$) (compared to <3.3 for $ta\text{-C}_{1-x}\text{:Gd}_x$). For $ta\text{-C}_{1-x}\text{:Gd}_x$ thin films, the starting matrix is highly sp^3 bonded ($>80\%$). After Gd implantation, there is no clear sign of development of a D peak with increasing x , but there is a strong monotonic decrease of Raman intensity with increasing Gd x to the extent that no reliable I_D/I_G ratio can be obtained for $x > 0.088$. The σ_{RT} of $ta\text{-C}_{1-x}\text{:Gd}_x$, like sputtered $a\text{-Gd}_x\text{C}_{1-x}$ films, increases with x for low concentration, indicating that Gd dopes both types of C matrices. σ_{RT} then decreases with x for both matrices (above a threshold concentration $x_{\text{th}} \approx 0.11$ for cosputtered $a\text{-Gd}_x\text{C}_{1-x}$ and 0.088 for Gd-implanted $ta\text{-C}$). In both cases, Raman data show that the reduced σ is due to changes in the carbon matrix, but the types of changes are quite different. In the sputtered films, a clear (inverse) correlation between

I_D/I_G and σ_{RT} is found $>x_{\text{th}}$. By contrast, no such correlation between I_D/I_G and x or σ_{RT} is found in $ta\text{-C}_{1-x}\text{:Gd}_x$. For $x \leq x_{\text{th}} = 0.088$, the implant-induced damage centers in the $ta\text{-C}$ matrix are not converted into graphitic sites (without RTA treatment); thus, σ increases with x but shows no dependence on I_D , the I_D/I_G ratio, or matrix graphitization. When $x > x_{\text{th}}$, the unknown Gd implant-induced damage centers (which are Raman inactive in the measured spectrum region and hence have no effect on I_D/I_G ratio) in the $ta\text{-C}$ matrix reduce conductivity, effects that compete with the increased carrier concentration associated with Gd doping and therefore cause a nonmonotonic dependence of σ on x .

Annealing (RTA treatment) of the implanted samples (both Gd and Xe) greatly increases $\sigma(T)$ for all x . This is due to bond rearrangement within damage centers, leading to a more conducting, graphitic matrix, as indicated by the development of D peaks (not seen in as-implanted $ta\text{-C}$ films, as shown in Fig. 3) in the Raman spectra upon annealing. Although the Raman spectra (which are sensitive only to the presence of D - and G -type structures and hence only indirectly to the sp^3 bonding) do not show a significant change for as-implanted samples, the implantation process has clearly already created damage centers that destabilize the sp^3 metastable bonds. These damage centers serve as precursors for sp^2 nucleation that develop upon annealing. Films become metallic due to these more conducting graphitic centers in the $a\text{-C}$ matrix. Also, on annealing, the MR ($= -MG$) becomes smaller due to the large increase of $\sigma(H = 0)$ in the denominator, even though the absolute change $\Delta\sigma$ increases.¹⁹

The high-field magnetic properties $M(H, T)$ of all the different Gd-doped amorphous semiconductors show similar behavior, with no sign of a magnetic phase transition but significant suppression below the Brillouin function at a lower temperature, even at quite high field, indicating strong frustrated Gd-Gd magnetic interactions. This frustration leads to SG freezing at higher Gd concentrations for all matrix types, with a freezing temperature that increases approximately linearly with increasing Gd concentration. Based both on the nature of the Gd $4f$ shell and on earlier work on Gd-Y-Si alloys, these interactions are an indirect carrier-mediated exchange, which we have called RKKY-like (the lack of crystallinity makes the theory somewhat different from the original RKKY theory). The degree of suppression in $M(H, T)$ below the Brillouin function indicates that these Gd-Gd interactions are strongest for $a\text{-Gd}_x\text{Si}_{1-x}$. This is likely due to a competition between the strength of the s (carrier)- f (local Gd moment) exchange interactions in the different local environments, directly related to the different MR, and the different atomic densities due to the different atomic sizes of C, Si, and Ge.

Despite the similarity in high-field $M(H, T)$, the low-field susceptibility $\chi(T)$ (analyzed above the SG freezing, if any) is significantly different for the different types of matrices. $\chi(T)$ data on both the present $ta\text{-C}\text{:Gd}$ samples and the previously reported sputtered $a\text{-Gd}_x\text{C}_{1-x}$ samples show a relatively simple CW law fit with an effective moment that is independent of x and somewhat greater than the $7.9 \mu_B$ of the $\text{Gd}^{3+} J = S = 7/2$ ion, as is commonly seen in Gd metallic alloys, and low θ values (near 0 K for low x and increasing to 5 K for higher x , still less than the freezing temperature). As a comparison, $\chi(T)$ data on $a\text{-Gd}_x\text{Si}_{1-x}$ samples also

show a near-CW-law dependence (low θ value), indicating that the Gd-Gd interactions, although extremely strong, are nearly perfectly balanced ferromagnetic and antiferromagnetic interactions but have an effective moment with a nontrivial dependence on composition, including a peak at the M - I transition. By contrast, $\chi(T)$ data for a -Gd $_x$ Ge $_{1-x}$ samples cannot be fit with a Curie (or CW) law; hence, no effective moment value can be extracted. However, $\chi(T)$ is quite small compared to both a -Gd $_x$ Si $_{1-x}$ and a -Gd $_x$ C $_{1-x}$ and is well fit to an A/T^α dependence, with $\alpha = 0.7$ for all x , a monotonic dependence of A on x , and no sign of the M - I transition.

These results show a systematic trend on changing from C, to Si, to Ge matrices from (for C) a relatively simple local Gd moment interacting via RKKY-like interactions and producing a small carrier polarization that adds to the effective moment of the Gd $^{3+}$ ions, as is often seen; to a material (Si), where the magnetic behavior is somewhat like traditional Gd alloys but with a moment-carrier interaction that results in a large and nontrivial x dependence of effective moment; and finally to a material (Ge), where the magnetic properties are nothing like the usual Gd-based systems. To the best of our knowledge, there is no theory for this systematic trend; we suggest that it results from the systematic drop in electron density (in reciprocal cubic centimeters) (for the same Gd concentration x) due to increasing atomic spacing/decreasing atomic number density (C-C distances being the smallest and Ge-Ge the largest), which causes changes in the nature of the carrier-local Gd $^{3+}$ moment interactions.

Turning now to a discussion of the magnetotransport, despite the types of C matrices, all Gd-doped a -C possess large negative MR at low T , with a magnitude that decreases exponentially with increasing T . The low- T , large negative MR is attributed to a magnetic disorder-induced carrier delocalization with increasing magnetic field; applying a magnetic field (partially) aligns the Gd moments, thus reducing the disorder seen by the transport carriers and leading to increased conductivity. The inset of Fig. 9 shows the magnitude of MR vs T for the $x = 0.07$ sample whose conductivity was shown in the main part of Fig. 9. This exponential dependence is similar to that previously found for both a -Gd $_x$ Si $_{1-x}$ and a -Gd $_x$ Ge $_{1-x}$, which have a negative MR that vanishes exponentially with increasing T and with increasing x (but is still measurable at 90 K). At low T , *small positive* MR is commonly found in *nonmagnetic* disordered electron systems due to electron correlation effects and *small negative* MR is found from elimination of quantum backscattering.²⁰

Figure 10 compares the T dependence of the negative MR for Gd doped in various matrices. The low- T negative MR (or positive MG) is of the same magnitude at a given x , T , and H as that for sputtered a -Gd $_x$ Si $_{1-x}$ and a -Gd $_x$ C $_{1-x}$, and is much larger than that for a -Gd $_x$ Ge $_{1-x}$ films. (The strongly insulating nature of most of the Gd-C samples precluded low- T MR measurements for all but the most conducting of these). The magnitude and temperature dependence of MR for the two types of Gd-C samples (the present implanted ta -C and the previous work on sputtered a -Gd-C alloys) are quite similar, deviating only above ~ 15 K; both have relatively similar x . The significant reduction in MR between a -Gd $_x$ Si $_{1-x}$ and a -Gd $_x$ Ge $_{1-x}$ was discussed in Ref. 6, where it was suggested to be associated with an increase in electron screening due to

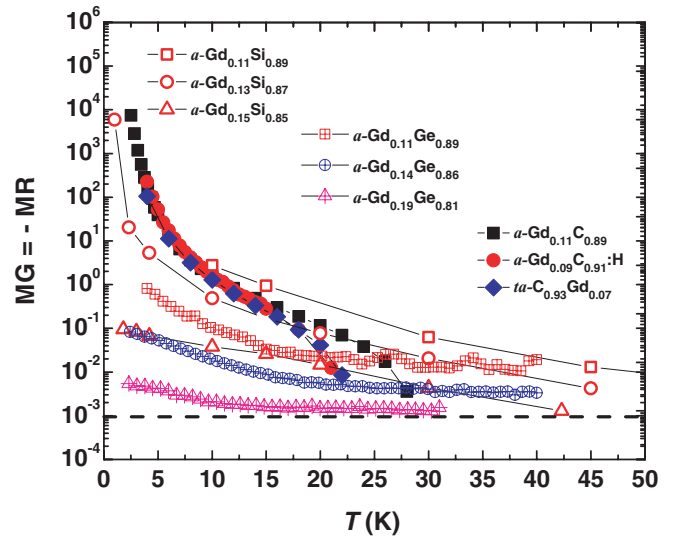


FIG. 10. (Color online) MG (negative MR) comparison among difference semiconductor hosts of the Gd dopant. The horizontal dashed line at $MG = 10^{-3}$ is shown as an example of an alternative definition of T' to that chosen in this paper.

the reduced band gap (and higher dielectric constant) of a -Ge; the present results suggest that screening effects are similar in ta -C $_{1-x}$ Gd $_x$, a -Gd $_x$ Si $_{1-x}$, and a -Gd $_x$ C $_{1-x}$ at low T and much weaker than those seen in a -Gd $_x$ Ge $_{1-x}$. In the carbon matrices, the magnetic properties $M(H, T)$ are closest to a simple model of local Gd $^{3+}$ moments interacting via RKKY-like interactions, with p_{eff} independent of x , suggesting that the carrier-moment interactions are local enough to be nearly unscreened.

Although the low- T MR behavior is similar, at *high* temperature, a -Gd-C samples show a small *positive* MR ($< 10\%$) with almost no T or x dependence, while a -Gd $_x$ Ge $_{1-x}$ has a low- T and x -independent negative MR and a -Gd $_x$ Si $_{1-x}$ has nearly zero MR at high T (meaning above ~ 100 K) for all x . For both a -Gd $_x$ Ge $_{1-x}$ and a -Gd $_x$ Si $_{1-x}$, it was possible to define a characteristic temperature below which the Gd moments affected electrical conductivity. This temperature could be defined either by some choice for a cutoff MR (e.g., 10^{-3} , 1%, or 10%) or by comparing zero-field $\sigma(T)$ to $\sigma(T)$ for non-magnetically doped analogues a -Y $_x$ Si $_{1-x}$ or a -Y $_x$ Ge $_{1-x}$.^{6,21} The latter method is effective for metallic samples ($x > 0.14$ in a -Gd $_x$ Si $_{1-x}$ and a -Gd $_x$ Ge $_{1-x}$), because it is a zero-field measurement and provides an unambiguous characteristic temperature, which we defined as T^* . However, this method is ineffective for insulating samples, briefly because the temperature dependence is not a simple power law and the dependence on x is far too strong to allow simple comparison to nonmagnetic analogs. The former method, based on MR, gives a temperature that we call T' ; T' depends on the magnitude chosen for the cutoff MR, but since MR vanishes exponentially with increasing temperature in both a -Gd $_x$ Ge $_{1-x}$ and a -Gd $_x$ Si $_{1-x}$, the choice is not significantly important. For a -Gd $_x$ Ge $_{1-x}$ and a -Gd $_x$ Si $_{1-x}$, T' is different from (lower than) T^* , but the dependence on x is the same.

In this work, all ta -C $_{1-x}$ Gd $_x$ samples are insulating, so T^* cannot be defined. Instead, by analogy to T' earlier, for all ta -C $_{1-x}$ Gd $_x$ films in this study, as well as in the previous

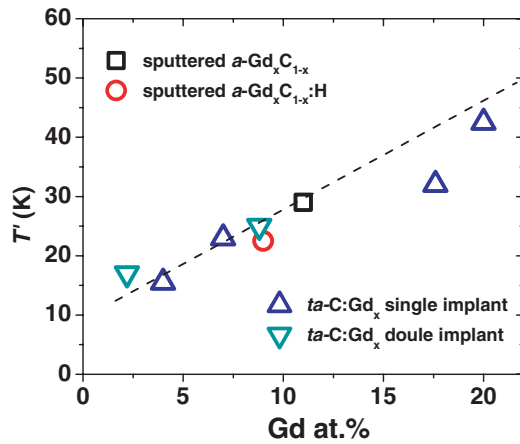


FIG. 11. (Color online) T' as a function of Gd doping x for different $a-C$ matrices, including sputtered $a-C(H)$ films and ion beam-deposited $ta-C$ films. MR can only be measured at low T for the most conductive samples, which are still on the insulating side of the $M-I$ transition. Alternative definitions of T' (e.g., $MG = 10^{-3}$) would not significantly change this plot.

work on sputtered $a-GdC_{1-x}$,⁷ we define T' as the temperature at which MR switches from positive to negative in a 70-kOe field; the Fig. 9 inset shows an example. (A cutoff of 10^{-3} for MR could equally well have been used to define MR.) This crossover temperature T' correlates perfectly with T^* for materials where both can be defined and plays a role similar to that of T^* ; i.e., it establishes a temperature scale below which Gd carrier-moment interactions dominate, causing the very large negative MR that dominates (in the C-based materials) the high- T , small positive MR.

Figure 11 shows T' as a function of x for $ta-C_{1-x}:Gd_x$, sputtered $a-Gd_xC_{1-x}$, and $a-Gd_xC_{1-x}:H$. Quite remarkably, T' shows a linear increase with x , independent of the details of C matrix type. This increase is in stark contrast to the decreasing T^* (and T'), with increasing x seen in $a-Gd_xSi_{1-x}$ and $a-Gd_xGe_{1-x}$, as well as ternary $a-Gd_xY_ySi_{1-x}$ alloys for constant x , and increasing y , which was interpreted as a consequence of increased screening of electron-moment interactions with the increasing metallicity associated with increasing x .²¹ The dependence on x seen in Fig. 11 suggests that screening plays little or no role in the T dependence of MR for $ta-C_{1-x}:Gd_x$ and sputtered $a-Gd_xC_{1-x}$, unlike its role in $a-Gd_xSi_{1-x}$ and $a-Gd_xGe_{1-x}$. We suggest that this is again an indication of a very local nature of the Gd moment-carrier interactions in the amorphous C-based systems, unlike Si and even more so Ge. In particular, again, the most obvious difference among the three matrices is their atomic density. For a given value of x , the measured Gd number density (Gd atoms per cubic centimeter) in $a-C$ is the highest, followed by $a-Si$, and then $a-Ge$. The carrier density in the impurity band of each is correspondingly highest for $a-C$, followed by $a-Si$, and then $a-Ge$, leading to our earlier comments on the cause of the increasingly local nature of the electron-moment interactions. Competing with this effect is the changing band gap, which decreases from C, to Si, to Ge; this increases electron screening due to virtual (not thermal) excitation of

carriers from the impurity band to the conduction band in these correlated electron materials near the $M-I$ transition.

V. CONCLUSIONS

$ta-C$ thin films with a high starting sp^3 fraction provide a new type of $a-C$ matrix for studying moment-carrier interactions when doped with the magnetic Gd ion. The MR of the $ta-C_{1-x}:Gd_x$ films is extremely large but does not exceed that of $a-Gd_xSi_{1-x}$, contrary to the expectation that the increased band gap of $ta-C$ would cause increased MR effects, including higher-temperature MR. This negative result is likely due to radiation damage to the sp^3 sites, a result that is enhanced by annealing, which causes further conversion to sp^2 bonding. For a given x , the magnitude of the negative MR below a crossover temperature T' for $ta-C_{1-x}:Gd_x$ is comparable to that for $a-Gd_xSi_{1-x}$ and larger than that for $a-Gd_xGe_{1-x}$. The crossover temperature T' , which indicates the strength of interactions, increases with Gd x , unlike what is seen in $a-Gd_xSi_{1-x}$, $a-Gd_xGe_{1-x}$, and ternary $a-Gd_xY_ySi_{1-x}$. This difference is suggested to be due to the extremely local unscreened nature of the carrier-moment interactions in Gd-C compared to the more extended interactions in Gd-Si and even more so in Gd-Ge. With quite different starting matrices and process conditions, implanted $ta-C_{1-x}:Gd_x$ and cosputtered $a-Gd_xC_{1-x}$ have little to no change in MR and magnetic properties. However, some differences are seen in the detailed transport properties, which can be explained by the differences in their Raman spectra.

Comparing the different group IV matrices, in both types of $a-C$, the Gd ions behave as large bare moments with little screening; they interact via RKKY-induced polarization of carriers, which produces a SG for high x , and have large negative MR due to interactions between well-defined local moments and carriers. In $a-Ge$, where the carrier concentration n (proportional to the atomic number density) is the lowest for a given Gd x and the band gap is the smallest, the magnetic properties of the Gd ion are significantly screened and the Gd-Ge interaction is weakened, leading to a small but still negative MR. In $a-Si$, where the carrier concentration is moderate, electron screening modifies the bare Gd moment but still leaves it behaving as a local moment, which produces extremely large MR. These changes in carrier-local moment interaction cause changes in the strength of the Gd-Gd interactions, with resulting changes in the $M(H,T)$. Overall, for all amorphous matrices (C, Si, and Ge), the Gd-Gd interactions remain strong, with mixed ferromagnetic and antiferromagnetic frustrated interactions. The systematic but nonmonotonic trends in these group-IV matrices suggest that electron concentration and band gap play separate important roles.

ACKNOWLEDGMENTS

We thank D. Queen for assistance in sample preparation. This research was supported by National Science Foundation Grant No. DMR-0505524. Raman spectroscopy work at the Lawrence Berkeley National Laboratory was supported by the director of the Office of Basic Energy Sciences, Materials Sciences and Engineering Division, of the US Department of Energy under Contract No. DE-AC02-05CH11231.

*li.zeng@gmail.com

- ¹C. Ronning, *Appl. Phys. A* **77**, 39 (2003).
- ²K. Bharuth-Ram, U. Vetter, H. Hofsäss, C. Ronning, and M. Dietrich, *Nucl. Instrum. Meth.* **190**, 835 (2002).
- ³S. Dhar, O. Brandt, M. Ramsteiner, V. F. Sapega, and K. H. Ploog, *Phys. Rev. Lett.* **94**, 037205 (2005).
- ⁴B. L. Zink, E. Janod, K. Allen, and F. Hellman, *Phys. Rev. Lett.* **83**, 2266 (1999).
- ⁵B. L. Zink, V. Preisler, D. R. Queen, and F. Hellman, *Phys. Rev. B* **66**, 195208 (2002).
- ⁶E. Helgren, F. Hellman, L. Zeng, N. Sinenian, R. Islam, and D. J. Smith, *Phys. Rev. B* **76**, 184440 (2007).
- ⁷L. Zeng, E. Helgren, F. Hellman, R. Islam, D. J. Smith, and J. W. Ager, *Phys. Rev. B* **75**, 235450 (2007).
- ⁸J. Robertson, *Mater. Sci. Eng. R* **37**, 129 (2002).
- ⁹H. Hofsäss, H. Binder, T. Klumpp, and E. Recknagel, *Diam. Relat. Mater.* **3**, 137 (1994).
- ¹⁰J. Ziegler, J. Biersack, and M. Ziegler, *Transport of Ions in Matter* (SRIM Co., Chester, Maryland, 2008).
- ¹¹L. R. Doolittle, *Nucl. Instrum. Meth.* **15**, 227 (1986).
- ¹²A. C. Ferrari and J. Robertson, *Phys. Rev. B* **61**, 14095 (2000).
- ¹³R. Kalish, Y. Lifshitz, K. Nugent, and S. Prawer, *Appl. Phys. Lett.* **74**, 2936 (1999).
- ¹⁴J. Wilks and E. Wilks, *Properties and Applications of Diamond* (Butterworth-Heinemann, Oxford, 1991).
- ¹⁵S. Prawer and R. Kalish, *Phys. Rev. B* **51**, 15711 (1995).
- ¹⁶F. Hellman, D. R. Queen, R. M. Potok, and B. L. Zink, *Phys. Rev. Lett.* **84**, 5411 (2000).
- ¹⁷V. Orlyanchik, M. B. Weissman, E. Helgren, L. Zeng, and F. Hellman, *Phys. Rev. B* **79**, 224402 (2009).
- ¹⁸L. Zeng, E. Helgren, F. Hellman, R. Islam, and D. J. Smith, *Phys. Rev. B* **75**, 184404 (2007).
- ¹⁹L. Zeng, E. Helgren, H. Zutz, C. Ronning, and F. Hellman, *MRS Symposia Proceedings*, Vol. 941 (Materials Research Society, San Francisco, CA, 2006), p. Q08.
- ²⁰P. A. Lee and T. V. Ramakrishnan, *Rev. Mod. Phys.* **57**, 287 (1985).
- ²¹E. Helgren, J. J. Cherry, L. Zeng, and F. Hellman, *Phys. Rev. B* **71**, 113203 (2005).